Supplement of Biogeosciences, 23, 3253–3277, 2026
https://doi.org/10.5194/bg-23-3253-2026-supplement

Biogeosciences Open Access EGU

Supplement of

Benthic phosphorus cycling in the northern Benguela upwelling system: excess P supply and altered pelagic nutrient stoichiometry

Peter Kraal et al.

Correspondence to: Peter Kraal (peter.kraal@nioz.nl)

12 pages

1 tables

11 Figures

S1. Total N and P measurements in water-column and pore-water samples

An unfiltered 10-mL water sample from a CTD-rosette bottle was directly transferred into a pre-rinsed 15-mL polypropylene centrifuge tube, the second 10-mL sample was filtered over an acid-cleaned 0.2-µm PES filter into a pre-rinsed 15-mL polypropylene centrifuge tube. These stations represent the contrasting depositional environments of the oxygenated slope (Station 2) and the strongly TOC-enriched shelf (Station 6). At NIOZ, these samples were analysed for total N and P by AA preceded by digestion of (particulate) organic compounds using persulfate oxidation and UV irradiation.

Analysis of total dissolved N and P in addition to DIN and HPO_4^{2-} in pore-water at stations 2 and 6 allowed the estimation of pore-water DON and DOP pools (Fig. S1). Total dissolved N and thus the DON pool was only quantified in pore-water from station 2, where it represented a significant dissolved N pool: 10–45 µmol L^{-1}, ~25–50 % of total dissolved N. Dissolved organic P was determined in station 2 and 6 pore-waters and was a much smaller pool than DON, both in absolute and relative terms. We first note that DOP, calculated as the difference between total dissolved P and HPO_4^{2-}, often resulted in negative numbers, indicating that there was no detectable DOP pool. This applied to most measured samples from station 6, where total dissolved P and HPO_4^{2-} concentrations were high, making a calculation by difference of a small P pool challenging. Where calculated DOP values were positive (mostly station 2 samples where P concentrations were relatively low), DOP ranged between 0.3 and 3.5 µmol L^{-1}, accounting for 1–10 % of total dissolved P.

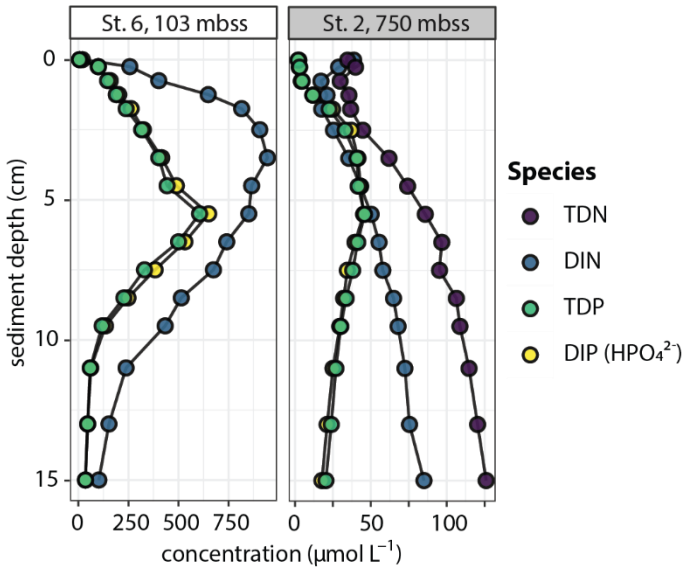

Figure S1: Pore-water profiles of total dissolved nitrogen (TDN), dissolved inorganic nitrogen (DIN), total dissolved phosphorus (TDP) and dissolved inorganic phosphorus (HPO_4^{2-}, or DIP) in pore-waters at stations 2 and 6. TDN for station 6 was not determined.

25

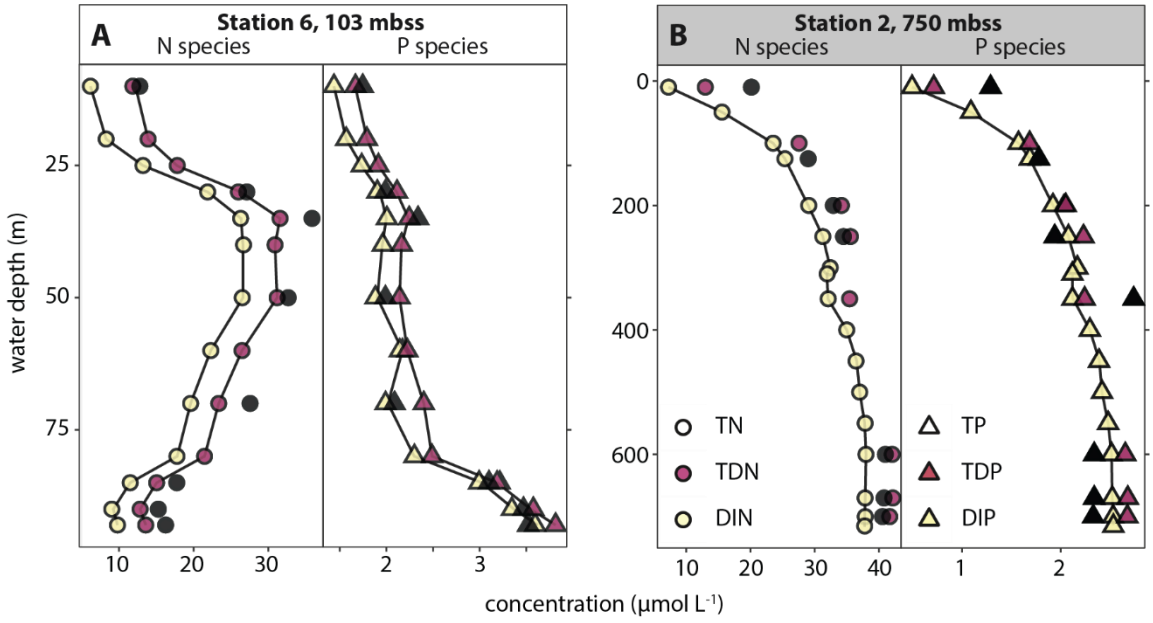

Figure S2: Water-column profiles of total (TN, TP), total dissolved (TDN, TDP) and total dissolved inorganic N and P (DIN, DIP).

S2. Dissolved oxygen micro-profiling at the sediment-water interface

For O_2 micro-profiling with micro-sensors, the readings of the microamperometer were converted to % air saturation using a temperature calibration at 100 % saturation (seawater bubbled with air for 20 min and then rested under very gentle stirring to avoid oversaturation).

Table S1. Temperature calibration of oxygen micro-sensor in seawater at 100% air saturation and atmospheric pressure.

Temp (°C)	Signal (pA)		
	1	*2*	*mean*
5	275	276	275.5
13	246	247	246.5
22	207	208	207.5

From this, we obtained: $nA_{100\%\ air\ sat} = -4.0069 * temp_{°C} + 296.6$ ($R^2 = 0.9974$). Taking the bottom-water temperature from the CTD measurements at each station, we calculated the maximum sensor response. Further, using standard relationships between O_2 concentration, temperature and salinity, we calculated the maximum bottom-water O_2 concentration in µmol L^{-1} for each station. Assuming a linear relationship between $[O_2]$ and sensor signal, we then obtained the O_2 micro-profiles in µmol L^{-1}. Using the O2 gradient in the diffusive boundary layer, we then calculated the diffusive sediment O_2 uptake (Jørgensen et al., 2022):

$$DBL\ flux = D \times \frac{dC}{dz} \quad \text{(S1)}$$

where D is the molecular diffusion coefficient of O_2 at the relevant temperature and salinity (calculated with the *marelac* package in Rstudio) and dC/dz is the vertical O_2 gradient.

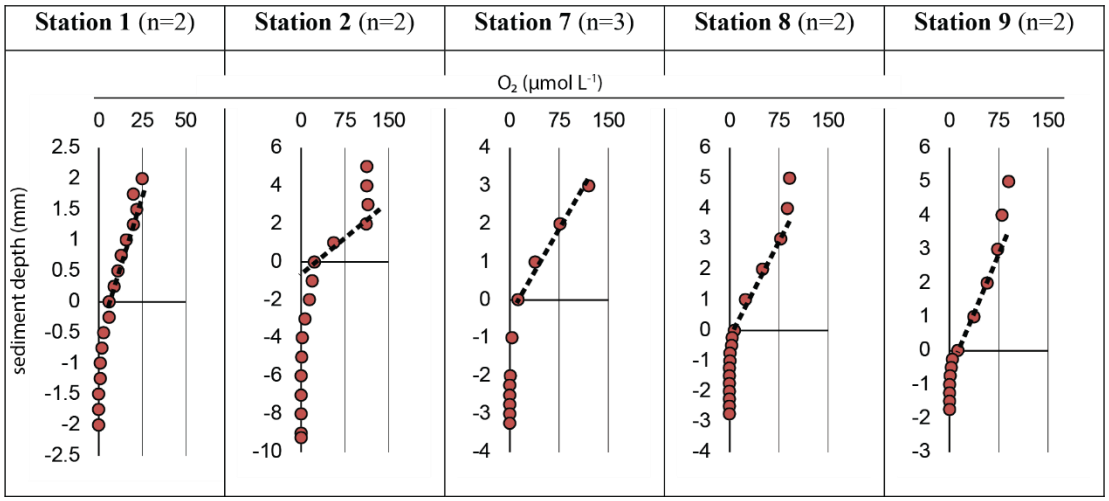

Figure S3. Dissolved O_2 micro-profiling around the sediment-water interface. No robust data could be collected for the stations on the oxygen-depleted shelf, likely due to intrusion of atmospheric oxygen. The thick black dashed line indicates the O_2 gradient around the SWI from which the diffusive O_2 uptake was calculated. Note that the unit of the y-axis, sediment depth, is in mm.

S3. Calculation of excess pore-water HPO_4^{2-}

With principles outlined in Burdige and Komada (2011) and adapted by Jilbert et al. (2020), we used the measured pore-water NH_4^+ profile to calculate the expected dissolved HPO_4^{2-} profile that would result from breakdown of algal organic matter with Redfield N/P stoichiometry (16) (Redfield, 1958) and simple accumulation of the released HPO_4^{2-} in the pore-water:

$$d\Delta NH_4^+ \Big/ d\Delta H_2PO_4^{2-} = -r_{N:P} \times D_{H_2PO_4^{2-}} \Big/ D_{NH_4^+}, \quad \text{(S2)}$$

where $d\Delta$[species] represents pore-water concentration gradient over depth, $r_{N:P}$ represents expected molar ratio of N:P in remineralized organic matter (assumed to be 16), and $D_{species}$ represents sediment diffusion coefficients of HPO_4^{2-} and NH_4^+, calculated at in situ temperature, salinity and pressure in R package marelac and corrected for sediment porosity.

S4. Visual observation of white, filamentous sulfur-oxidizing bacteria

Figure S4. Images of white filamentous microbes, likely sulfur-oxidizing bacteria, observed in core tops from stations 4, 5 and 6 on the oxygen-depleted shelf (~ 100 – 105 mbss). The middle image shows occurrence up to a few centimetres into the sediment.

S5. Correlations between benthic fluxes

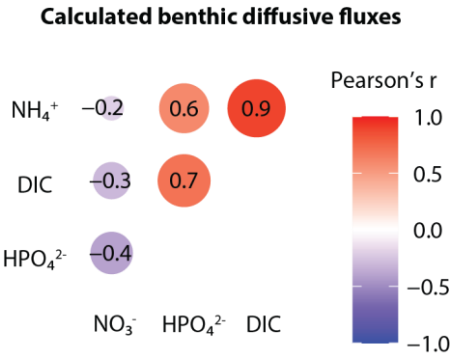

Figure S5. Correlation matrix for calculated diffusive benthic fluxes of C, N and P.

S6. Whole-core incubations and benthic fluxes

S6.1 Time series of C, N and P in the overlying water

The consumption or accumulation of key dissolved species over time in whole-core incubations was determined by taking discrete, filtered samples of the overlying water over time. Low-quality data was already pruned from this dataset prior to further processing. For flux calculations, subsequently a threshold R^2 of ±0.3 was applied to discard time series that did not show a robust increasing or decreasing trend.

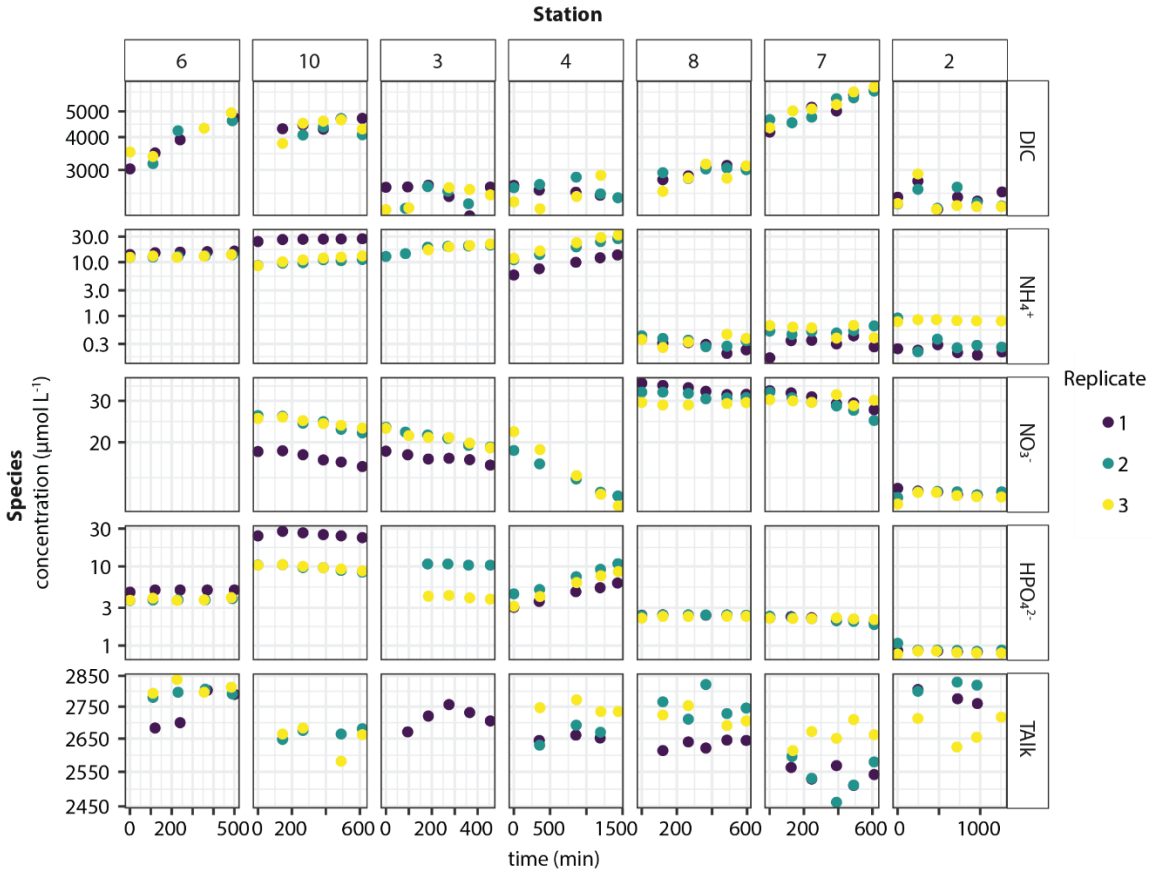

Figure S6. Time series of concentrations of key species in overlying water during whole-core incubations.

S6.2 Time series of dissolved O_2 in the overlying water

Dissolved O_2 in the overlying water during whole-core incubation at selected stations was monitored at high temporal resolution (every 2 minutes) using a Presens fiber optic system. Limited reliable data were gathered from the triplicate cores, particularly for shelf stations where bottom-water oxygen was (very) low. Below, we show data for station with more or less

oxygenated bottom waters. For station 3, we the O_2 time series showed relatively high concentrations (starting from 20-25% air saturation while bottom water was ~5% air-saturated), which indicates that O_2 had entered the incubation cores during preparation of the incubation experiment. These higher O_2 levels may have stimulated oxic respiration and the O_2 consumption rate for station 3 is therefore treated with caution. We note that the resulting O_2 of ~15 mmol m^{-2} d^{-1} is similar to rates found on the Namibian shelf during in-situ incubation (Chuang et al., 2022).

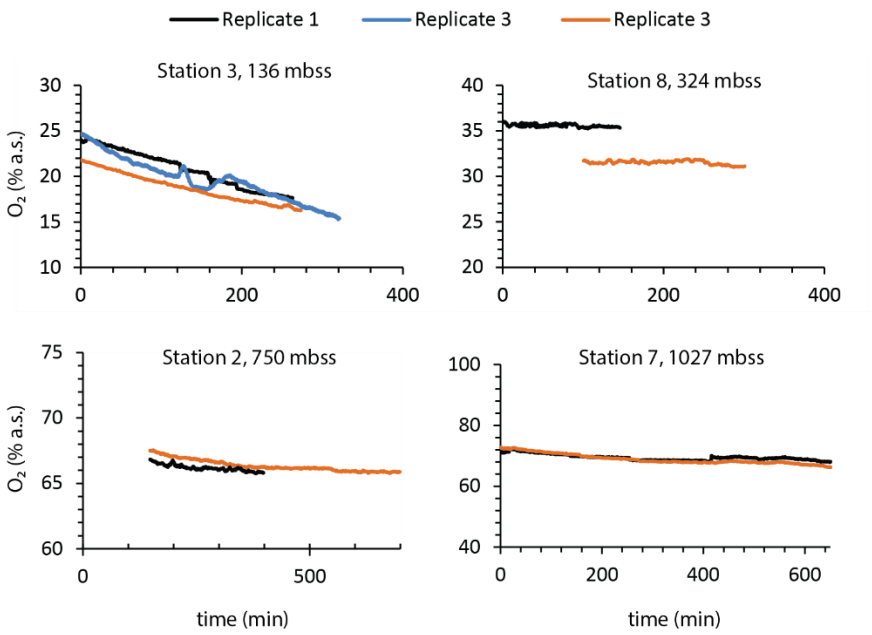

Figure S7. Time series of dissolved O_2 in overlying water during whole-core incubations.

S6.3 Whole-core and diffusive flux calculations

Concentration changes of O_2, DIC, TAlk, NH_4^+, NO_3^- and HPO_4^{2-} in the overlying water in combination with elapsed time, sediment area and volume of overlying water were used to calculate whole-core (total) benthic fluxes:

$$F_i = {}^{\Delta C}/_{\Delta t} \times {}^{V}/_{A} \quad \text{(S3)}$$

where F_i is the measured flux of analyte i (mmol m^{-2} d^{-1}), $\Delta C/\Delta t$ is the rate of concentration change (µmol L^{-1} d^{-1}) measured in the overlying water, V is the volume of overlying water (dm^3), and A is the area of sediment surface in the core (dm^2).

Measured whole-core-incubation fluxes of DIC, TAlk, NH_4^+, NO_3^- and HPO_4^{2-} were compared to diffusive fluxes calculated using pore-water and bottom-water profiles for selected elements with Fick's First Law:

$$J_i = -\varphi \times D_{sed} \times {}^{\delta C}/_{\delta z} \quad \text{(S4)}$$

where J_i is the calculated diffusive flux of the element i (mmol m^{-2} d^{-1}); φ is the sediment porosity (cm^3 cm^{-3}) calculated from gravimetric water content; D_{sed} is the sediment diffusion coefficient for the analyte at ambient temperature (s cm^{-2}), pressure and salinity calculated using the *R* package *marelac* corrected for sediment tortuosity (Burdige, 2006); δC/δz is the concentration gradient across the sediment-water interface (mmol cm^{-4}). The latter was calculated from the analyte's concentration in the bottom water (overlying water) and first pore-water sample (0.5 cm sediment depth). As described in S1, diffusive O_2 fluxes were calculated using the obtained micro-profiles across the SWI.

The diffusive DIC fluxes were similar to oxygen and sulphate consumption rates, respectively, on the shelf (9–25 mmol m^{-2} d^{-1}) and slope (-2–8 mmol m^{-2} d^{-1}).

S6.4 Whole-core and diffusive DIC and TAlk fluxes

The diffusive DIC fluxes were similar to oxygen and sulphate consumption rates, respectively, on the shelf (9–25 mmol m^{-2} d^{-1}) and slope (-2–8 mmol m^{-2} d^{-1}). The DIC and TAlk fluxes were similar, except at station 6 where the diffusive TAlk flux (50 mmol m^{-2} d^{-1}) was much larger than the DIC flux (24 mmol m^{-2} d^{-1}). There was a marked difference between the calculated and measured DIC fluxes with highly variable measured DIC fluxes that were particularly high for stations 6 and 7 (100 – 1500 mmol m^{-2} d^{-1}). The accompanying TAlk fluxes were about an order of magnitude lower.

The DIC fluxes were up to two orders of magnitude higher than calculated fluxes and those measured in other upwelling areas, particularly at stations 6, 10 and 7. Furthermore, diffusive fluxes of TAlk were similar to diffusive DIC fluxes but measured TAlk fluxes were one or two orders of magnitude lower. These extremely high DIC fluxes seem robust as they were similar in triplicate corer incubations (see also Fig. S6) but are difficult to explain. The observation that DIC fluxes far exceed TAlk fluxes makes $CaCO_3$ dissolution unlikely, rather it suggests that aerobic OM degradation and associated CO_2 production plays an important role in shaping the DIC flux. We note that stations 6 and 7, with the highest DIC fluxes, also show the strongest dissolved H_4SiO_4 enrichment in the bottom water; we propose that this may indicate a role for localized deposition and rapid degradation of sinking diatoms. Sediment chemistry and TOC content on the NBUS shelf is strongly impacted by the deposition of dead biomass from diatom blooms (Calvert and Price, 1983; Bremner, 1978; Borchers et al., 2005).

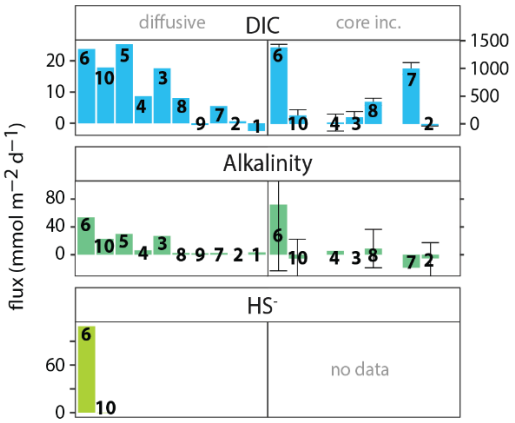

Fig. S8: Benthic fluxes of DIC, TAlk and HS^- across the sediment-water interface: negative fluxes are directed into the sediment, positive fluxes are directed into the bottom water. Left panels: calculated fluxes using concentration gradient in the diffusive boundary layer (O_2) or the gradient between bottom water and uppermost pore-water sample at 0.25 cm depth (all other species). Right panels: measured benthic fluxes calculated from changes in bottom-water chemistry during whole-core incubations. For measured fluxes, mean values and standard deviation of replicate core incubations are shown.

S7. Bottom-water chemistry

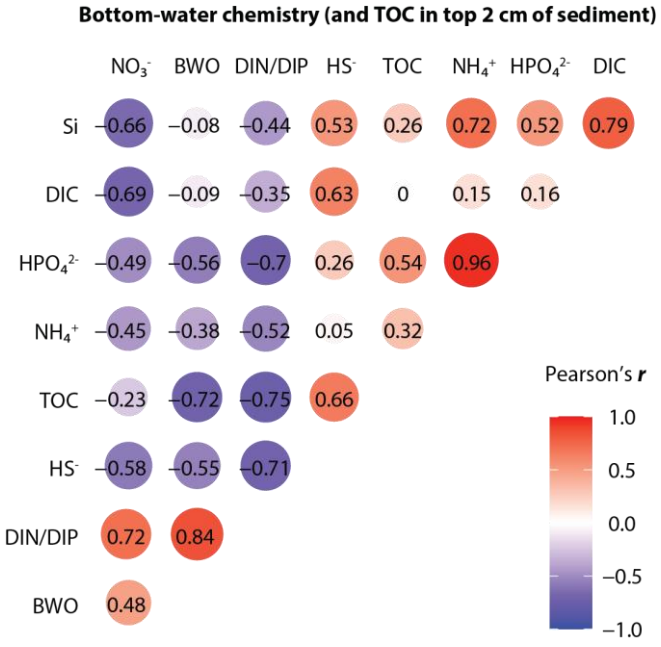

Figure S9. Correlation plot for bottom-water parameters and TOC content in the top 2 cm of the sediment.

S8. ^{31}P-NMR results

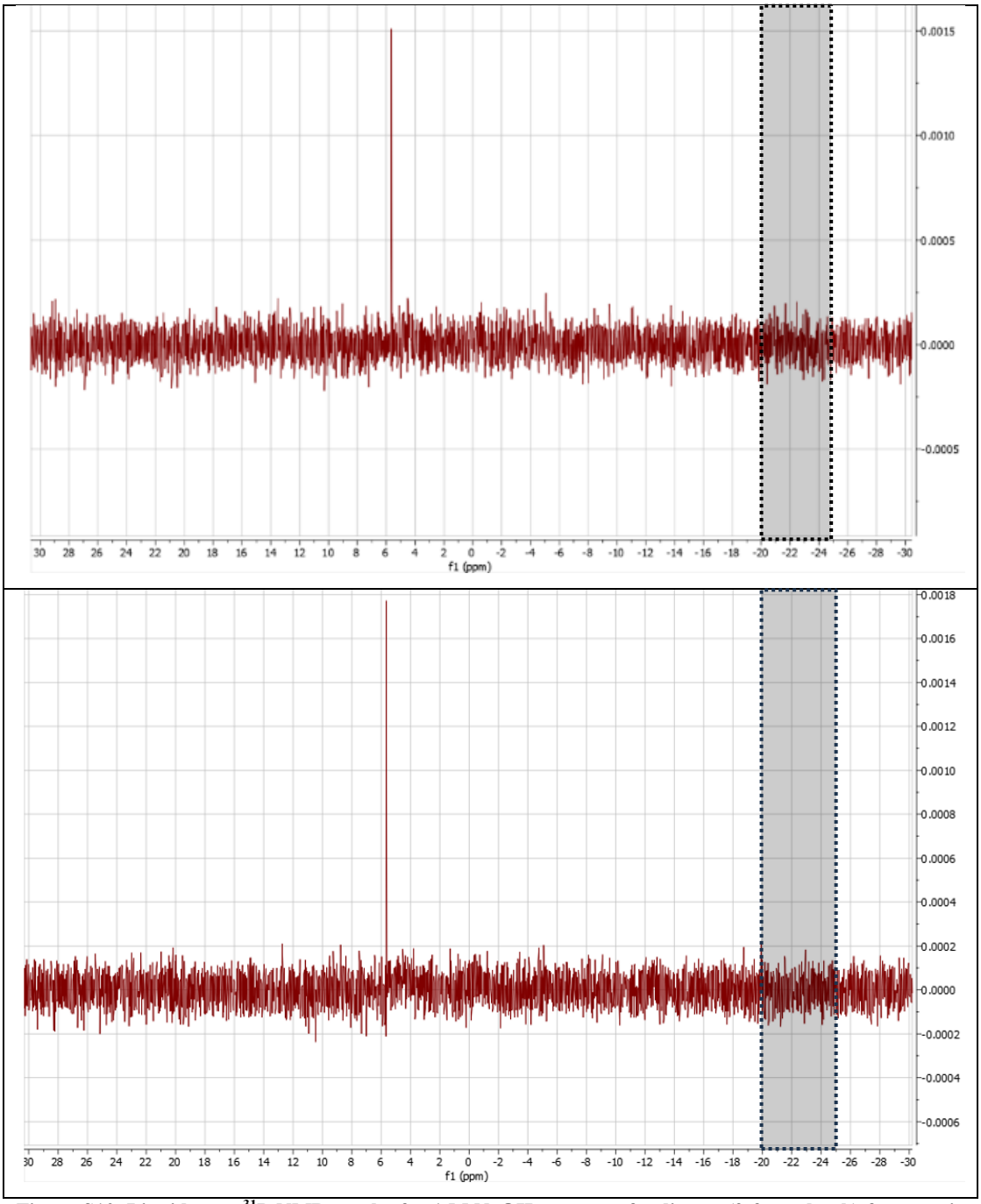

Figure S10. Liquid-state ^{31}P-NMR results for 1 M NaOH extracts of sediment (2-3 cm depth) from station 6 (top) and 2 (bottom). An orthophosphate peak is clearly visible at ~ 6 ppm, no evidence for poly-P which would be expressed as peaks around -20 – -25 ppm (indicated by grey area with dashed outline).

S9. Genetic analysis and results

DNA samples from station 2 (0–2 cm), station 4 (0–1 cm), station 6 (0–1 cm), and station 7 (0–1 cm) were extracted using the DNeasy PowerSoil Pro Kit (QIAGEN, Germany) following the manufacturer's instructions. Extracted DNA was pooled per station and was used for microbial community profiling through 16S rRNA gene amplicon sequencing using a Bacterial 16S rRNA gene primer set targeting the V3-V4 region (357F: TACGGGAGGCAGCAG / 800R: CCAGGGTATCTAATCC) (Kisand et al., 2002; Turner et al., 1999). Amplicon libraries were sequenced using Illumina MiSeq technology with a 2 × 250 bp paired end read configuration. Sequence data were processed using the CASCABEL pipeline (Abdala Asbun et al., 2020), with quality control, denoising, and chimera removal, and identification of amplicon sequence variants (ASVs). Taxonomic assignment was performed on the resulting chimera-free ASVs using the assignTaxonomy function in DADA2, and the classifier was trained against the SILVA reference database, specifically version NR99, v.138.1. Results are shown in Fig. S8, below. There were no counts in any of the sample extracts for the order of Thiotrichales, to which sulfide-oxidizing bacteria such as Thiomargarita, Thioploca and Beggiatoa belong.

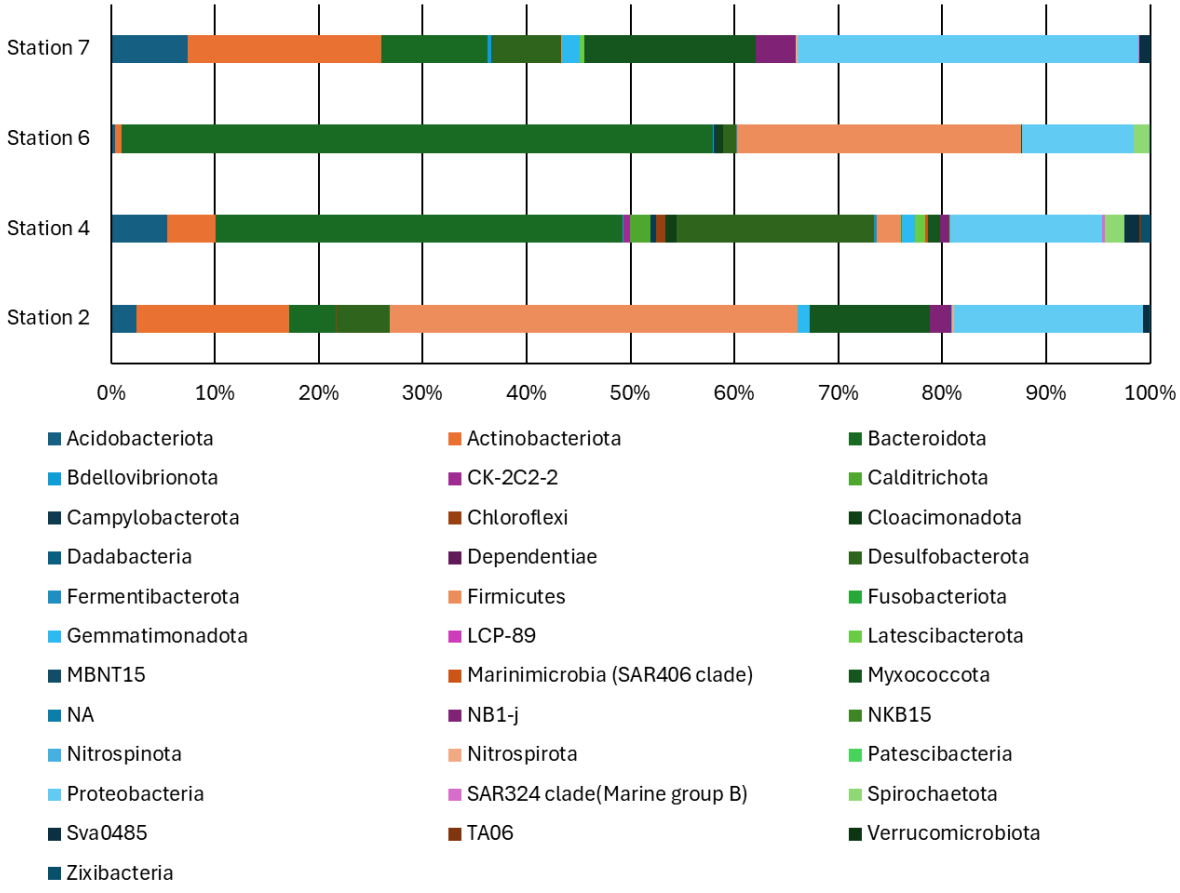

Fig. S11. Genetic results for selected surface samples from the shelf (station 4, 6) and the slope below the perennial OMZ (station 2, 7).

References

Borchers, S. L., Schnetger, B., Böning, P., and Brumsack, H.-J.: Geochemical signatures of the Namibian diatom belt: Perennial upwelling and intermittent anoxia, Geochem, Geophys. Geosyst., 6, doi:10.1029/2004GC000886, 2005.

Bremner, J. M.: Sediments on the continental margin off South West Africa between latitudes 17º and 25º S, 1978.

Burdige, D. J.: Geochemistry of marine sediments, Princeton University Press2006.

Burdige, D. J. and Komada, T.: Anaerobic oxidation of methane and the stoichiometry of remineralization processes in continental margin sediments, Limnol. Oceanogr., 56, 1781–1796, https://doi.org/10.4319/lo.2011.56.5.1781, 2011.

Calvert, S. E. and Price, N. B.: Geochemistry of Namibian Shelf Sediments, in: Coastal Upwelling Its Sediment Record: Part A: Responses of the Sedimentary Regime to Present Coastal Upwelling, edited by: Suess, E., and Thiede, J., Springer US, Boston, MA, 337–375, 10.1007/978-1-4615-6651-9_17, 1983.

Chuang, P.-C., Anderson, C. H., Kossack, M., Fabian, J., Su, C.-C., Vosteen, P., Zabel, M., Scholz, F., Schulz-Vogt, H. N., Sommer, S., and Dale, A. W.: Nutrient turnover by large sulfur bacteria on the Namibian mud belt during the low productivity season, Frontiers in Marine Science, Volume 9 - 2022, 10.3389/fmars.2022.929913, 2022.

Jilbert, T., Jokinen, S., Saarinen, T., Mattus-Kumpunen, U., Simojoki, A., Saarni, S., Salminen, S., Niemistö, J., and Horppila, J.: Impacts of a deep reactive layer on sedimentary phosphorus dynamics in a boreal lake recovering from eutrophication, Hydrobiologia, 847, 4401–4423, 10.1007/s10750-020-04289-9, 2020.

Jørgensen, B. B., Wenzhöfer, F., Egger, M., and Glud, R. N.: Sediment oxygen consumption: Role in the global marine carbon cycle, Earth-Sci. Rev., 228, 103987, https://doi.org/10.1016/j.earscirev.2022.103987, 2022.

Kisand, V., Cuadros, R., and Wikner, J.: Phylogeny of culturable estuarine bacteria catabolizing riverine organic matter in the northern Baltic Sea, Appl. Environ. Microb., 68, 379–388, 10.1128/aem.68.1.379-388.2002, 2002.

Redfield, A. C.: The biological control of chemical factors in the environment, Am. Sci., 46, 205–222, 1958.

Turner, S., Pryer, K. M., Miao, V. P., and Palmer, J. D.: Investigating deep phylogenetic relationships among cyanobacteria and plastids by small subunit rRNA sequence analysis, J Eukaryot Microbiol, 46, 327–338, 10.1111/j.1550-7408.1999.tb04612.x, 1999.